ACS OMEGA

http://pubs.acs.org/journal/acsodf

Article

Adsorption of 4-Mercapto Pyridine with Gold Nanoparticles Embedded in the Langmuir−Blodgett Film Matrix of Stearic Acid: SERS, XPS Studies Aided by Born−Oppenheimer on the Fly Dynamics, Time−Resolved Wavelet Transform Theory, and DFT

Somsubhra Saha,[‖] Bipan Dutta,[‖] Manash Ghosh, and Joydeep Chowdhury*

Cite This: *ACS Omega* 2022, 7, 27818−27830

Read Online

ACCESS | Metrics & More | Article Recommendations | Supporting Information

ABSTRACT: This paper reports the adsorptive behavior of the 4-mercaptopyridine (4MPy) molecule soaked in gold nanoparticles (AuNPs) that remain embedded in the bilayer Langmuir−Blodgett (LB) film matrix of stearic acid (SA) for various soaking times (STs). The as-fabricated substrate proved to be an efficient SERS sensing platform that can sense the analyte 4MPy molecules at trace concentrations of ~1.0×10^{-9} M. The XPS study not only reveals the adsorption of 4Mpy molecules with AuNPs via a sulfur atom but also suggests partial degradation of the analyte molecule upon adsorption. This observation is further substantiated from the SERS spectral profile, which shows unusual broadening of the enhanced Raman bands of the molecule at higher STs. The experimental observations are supported by Born−Oppenheimer on-the-fly molecular dynamics (BO-OF-MD), time-resolved wavelet transform theory (WT), and the DFT calculations based on adcluster models. Selective enhancements of Raman bands in the SERS spectra further suggest the involvement of charge transfer (CT) interaction to the overall enhancements of Raman bands of the analyte molecule. The molecule → CT contribution has been estimated from electron density difference calculations and the corresponding CT distance; the amount of CT is also envisaged.

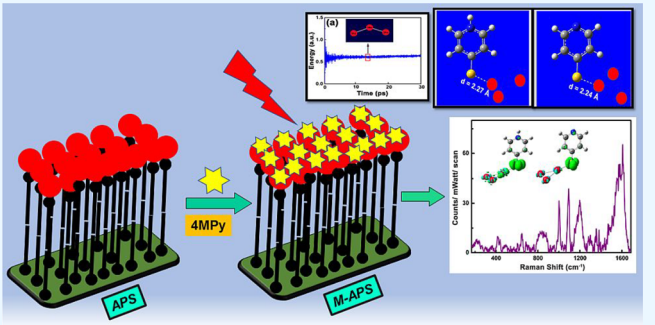

1. INTRODUCTION

Surface-enhanced Raman scattering (SERS) spectroscopy[1] has opened up new horizons not only in the offing of analytical sciences but also in elucidating the physics and chemistry of the surfaces.[2−7] Although the underlying reason behind colossal enhancements in the Raman signals has now been unanimously acclaimed to originate broadly from electromagnetic (EM) and charge transfer (CT) mechanisms, there however has been renewed interest in fabricating new SERS active substrates and understanding their adsorptive behaviors with the aid of improved adatom models.[8−11] While fabrications of new SERS active substrates that offer promising applications in the real-world diagnostics and in forensic sciences have gained significant attention from material scientists these days,[12−15] improved ad-cluster molecule−metal (M_n, n = 1 to 20) models from quantum chemical calculations proved to be effective in understanding their adsorptive behaviors.[16−21]

Considering the above issues, the present paper reports facile fabrication of a SERS active substrate through integration of self-assembly and Langmuir−Blodgett (LB) deposition techniques. Efficacy of the as-fabricated substrate has been tested from the SERS spectra of the analyte 4-mercaptopyridine (4MPy) molecule. The adsorptive site of the analyte molecule with the substrate has been investigated in detail from X-ray photoelectron spectroscopy (XPS) studies. The experimental observations are aided by Born−Oppenheimer on-the-fly molecular dynamics (BO-OF-MD), time-resolved wavelet transform theory, and density functional theory (DFT) calculations based on analyte molecule−metal adcluster models. To the best of our knowledge, this paper may be considered the first ever report where the most probable molecule−adcluster model has been proposed from BO-OF-MD followed by DFT calculations. The CT contribution to the overall enhancement of the SERS spectra of the 4MPy molecule has also been envisaged from electron density difference (EDD) studies.

Received: December 28, 2021
Accepted: May 5, 2022
Published: August 2, 2022

2. EXPERIMENTAL PROCEDURE

2.1. Materials and Methods. Spectroscopic grade 4MPy molecule, ∼95% purity; stearic acid (SA), >99% purity; and chloroauric acid ($HAuCl_4$), 99.995% purity were purchased from Sigma-Aldrich and were used as received. Trisodium citrate (∼99% purity), ethanol (>99% purity), and acetone (≥99% purity) were purchased from E-Merck (Germany) and were used without further purification. Spectral grade chloroform was purchased from SRL India and was used as received. The glassware used in the entire course of the experiment was vigorously cleaned with freshly prepared aqua regia, rinsed with distilled water, and dried in a hot oven before use. All of the required solutions were prepared using triple distilled deionized water (∼18.2 MΩ cm resistivity and pH ∼ 6.8) from the Milli-Q-plus system from Millipore Corporation, USA.

Quasi-spherical gold nanocolloids (AuNCs) of an average particle size of ∼55 nm in diameter were synthesized by a citrate reduction method following the recipe proposed by Frens.[22,23] The bilayer LB films of SA were lifted on the precleaned quartz substrates by the Y-type deposition technique using a computer controlled LB trough (Model No. D2007) manufactured by the "Apex Instruments". Chloroform was used as a solvent which readily dissolves SA. The subphase of the LB trough was filled with triple distilled deionized water. The pressure−area (π−A) isotherm plot of SA was estimated with a film balance, and the surface pressure was calibrated by the Wilhelmy plate using filter paper. About 80 μL of SA in chloroform solvent (∼1 mg/mL) was slowly and carefully dispensed with the help of a microsyringe at the air−water interface of the LB trough. The chloroform solvent was then allowed to evaporate by keeping the system undisturbed for 20 min. Evaporations of the solvent molecules eventually allow the amphiphilic SAs to settle as a floating monolayer at the air−water interface on the LB trough. The floating SA molecules in the LB trough were compressed by slowly moving the barrier at a constant speed of 2 mm/min. The π−A isotherm plot was monitored during the entirety of the compression steps. The LB film of SA was then dipped in AuNCs for 24 h and finally dried in a hot air oven to remove the excess metal ions from the surface of the film. We designate this final LB film substrate accomplished after dipping in AuNC as the "as prepared substrate" (APS).

2.2. Instrumentation. The UV−vis electronic absorption spectra of AuNC, APS, and the APS soaked in an aqueous solution (1.0×10^{-9} M) of 4MPy were recorded using a Jasco UV−vis absorption spectrometer (model no: V-630). The absorption spectra of AuNC and APS were recorded directly from the colloidal suspension and from the LB film substrate, respectively. The electronic absorption spectra of the APS substrates after being soaked in the 4MPy solution for 1, 1.5, and 2 h were also recorded from the modified LB film substrates. The normal Raman (NR) and the surface enhanced Raman scattering (SERS) spectra were recorded with a J-Y Horiba Confocal Triple Raman Spectrometer (Model: T 64000) fitted with gratings of 1800 groove/mm and a TE cooled Synapse CCD detector from J-Y Horiba. An aliquot containing 50 μL of aqueous solution of 1 M 4MPy was drop-casted on a quartz slide and was allowed to dry before recording the NR spectrum. For SERS measurements, the gold nanoparticles (AuNPs) embedded in the LB film substrates of SA were soaked in 1.0×10^{-9} M aqueous solution of 4MPy for 1, 1.5, and 2 h. The substrates were then removed from the solution and allowed to dry before recording the SERS spectra. The samples were then excited using a 632.8 nm red line of the He−Ne laser [Spectra Physics, USA (Model.Stabilite2017)] with a spot diameter and laser power of ∼1 μm and ∼60 μW, respectively. The scattered signals were collected at a 180° scattering angle to the excitations from an Olympus open stage microscope of 50× objective. The detector and the data acquisition were controlled by Lab Spec 5 software as provided by Horiba. The acquisition times for recording both the NR and SERS spectra were fixed at 20 s. The surface morphology of the LB films was recorded from FESEM (JEOL JSM 7600F) at 15 kV excitation energy. The AFM studies were accomplished using the NTEGRA system with a resolution of 1 nm from NT-MDT Spectrum Instruments. The XPS analyses have been performed on the as-prepared SERS active substrates with an ULVAC PHI 5000 Versa Probe-II, operating at 1.6×10^{-6} Pascals of pressure. An Al Kα ($h\upsilon$ = 1486.6 eV) X-ray source with a fixed operating power at 25 W and X-ray focus area 100 μm in diameter was used as a source to irradiate the substrates. The binding energy scales were calibrated from the C 1s photoelectron peak centered at ∼284.8 eV. The narrow scan XPS spectra were recorded using an analyzer pass energy of 58.7 eV with an energy step size of 0.125 eV.

2.3. Computational Details. The BO-OF-MD simulations had been carried out using the CPMD program operated in a Linux environment.[24] The 4Mpy molecule and bulk gold (Au) atoms with $\rho_{Au} \sim 19.32$ g/cm^3 [25] were placed in a simple cubic cell of dimensions 10.0 Å. Periodic boundary conditions were applied on the cell with 10 Å edges to ensure no appreciable interactions between the periodic images. The BO-OF-MD simulations were then executed in the NVT ensemble at room temperature over an equilibrium time of 30 ps. The time step was set to ∼0.1 fs. The temperature of the ensemble was controlled through a Nose−Hoover thermostat.[26,27] The gradient corrected Perdew, Burke, and Ernzerhof (PBE) functional[28] had been utilized to model the electronic exchange and correlation factors. Core electrons were treated with the pseudopotentials of Troullier and Martins,[29] while valence electrons were represented by a plane-wave basis set truncated at an extended energy cutoff of 80 Ry. The simulated data and the respective snap shots were visualized using the VMD[30] visualization software.

The DFT calculations were accomplished using the Gaussian-09 suite of software[31] using the B3LYP[32,33] exchange correlation functional. For structural optimizations and calculations of vibrational frequencies, the 6-31++g(d,p) basis was used for the light elements (C, H, N, and S) of the 4MPy molecule. For gold cluster models, the valence and the core electrons of Au atoms were defined by the pseudopotential LANL2DZ basis set. The vibrational frequencies of the respective molecule−metal cluster models, so attained using the B3LYP/6-31++g(d,p) [for C, H, N, and S]/LANL2DZ (for Au atoms) level of theory, had been scaled with a scaling factor 0.98. In the process of geometry optimization for the fully relaxed method with very tight criteria, convergence of all of the calculations without any imaginary values in the vibrational frequencies presage the accomplishment of local minima on the potential energy surfaces. The electron densities of the 4Mpy molecule and the Au atoms have been calculated using the B3LYP/6-31++g(d,p) [for C, H, N, and S] and B3LYP/LANL2DZ levels of theory, respectively. However, for the molecule−metal cluster

https://doi.org/10.1021/acsomega.1c07321
ACS Omega 2022, 7, 27818−27830

models, the electron density differences (EDD) have been estimated using the B3LYP/6-31++g(d,p) [for C, H, N, and S]/LANL2DZ (for Au atoms) level of theory.

The intensities of the Raman bands (I_{Raman}) have been estimated from the differential Raman scattering cross section (DRSC) ($^{d\sigma}/_{d\Omega}$) values using the following expression:[34−36]

$$I_{\text{Raman}} = \left(\frac{d\sigma}{d\Omega}\right)_i = \frac{(2\pi)^4}{45}\frac{h}{8\pi^2 c\omega_i}\frac{(\omega_0 - \omega_i)^4}{1 - \exp(-hc\omega_i/k_B T)}S_i \quad (1)$$

where σ and Ω signify the scattering cross section and the solid angle at which the scattered light signal is collected, while h, c, k_B, and T represent the Planck constant, speed of light, Boltzmann constant, and Kelvin temperature, respectively. The frequencies (in cm^{-1}) of the incident light and the "ith" vibrational mode are depicted by ω_0 and ω_i, respectively. The Raman scattering factor (Å^4/amu) for the "ith" normal mode of vibration is expressed as

$$S_i = 45\left(\frac{d\alpha}{dQ_i}\right)^2 + 7\left(\frac{d\gamma}{dQ_i}\right)^2$$

where ($^{d\alpha}/_{dQ_i}$) and ($^{d\gamma}/_{dQ_i}$) represent the derivatives of the isotropic and anisotropic polarizabilities α and γ with respect to the "Q_ith" normal mode, respectively.

The 4-mercaptopyridine (4MPy) molecule is reported to exist in protonated−deprotonated and in thiol−thione tautomeric forms at neutral pH (pH ∼ 7).[37,38] However, from our earlier study[39] and from the studies reported elsewhere,[37,38,40,41] it is seen that, in the surface adsorbed state, 4MPy molecules exist in the protonated thione (4MPyH) as well as in the deprotonated thione (4MPyD) forms at neutral pH (pH ∼ 7). The wavelet transform (WT) theory had thus been applied to estimate the time-resolved vibrational spectra for both 4MPyH and 4MPyD forms of the 4MPy molecule in the presence of a Au cluster system using the BO-OF-MD calculations. The vibrational signatures of 4MPyH and 4MPyD in the vicinity of the Au cluster were obtained from the Fourier transform of the trajectories so generated from the BO-OF-MD calculations.[36] The stretching distances of atoms as a function of time linked with the vibrational modes of the molecule were elicited from the BO-OF-MD trajectories. The VDOS of the corresponding normal modes were then attained with the aid of Fourier transformation. Thereafter, the wavelet transform was applied for the estimation of frequency as a function of time for individual vibrational modes of the molecule.

The wavelet transform $W_n(s)$ in the reciprocal space is expressed as[36]

$$W_n(s) = \sum_{k=1}^{n-1} \hat{F}_k \hat{\psi}(s\omega_k) e^{i\omega_k n\delta t} \quad (2)$$

where ω_k represents the angular frequency for the kth normal mode and F_k and $\hat{\psi}$ are the Fourier transformations of the time series F_n and the mother wavelet $\psi(t)$, respectively. The mother wavelet $\psi(t)$ is represented as[42]

$$\psi(t) = \pi^{-1/4} e^{i\omega_0 t - t^2/2\sigma^2} \quad (3)$$

Here, the parameters ω_0 and σ are considered from previous literature.[36,43] Successful applications of the above functional form of the mother wavelet $\psi(t)$ as reported elsewhere and are known to reproduce the Fourier power spectrum accurately.[36,42−44]

3. RESULTS AND DISCUSSIONS

The room temperature surface pressure (π)−area (A) isotherm plot of SA is shown in Figure S1 under section S1 of the Supporting Information.

3.1. UV−Vis Electronic Absorption Spectra of the AuNC and APS. The room-temperature UV−vis absorption spectrum of the as synthesized AuNC is shown in Figure 1.

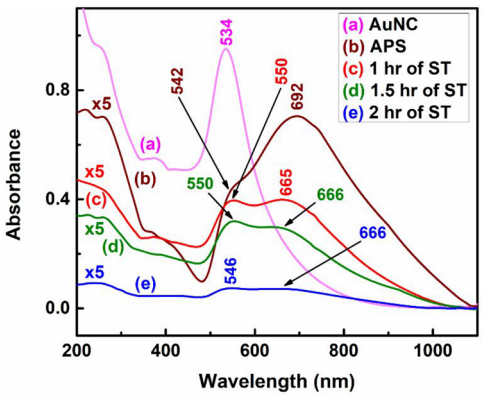

Figure 1. Room temperature UV−vis electronic absorption spectra of (a) AuNC (pink trace); (b) the APS (brown trace) and the modified M-APS so attained after (c) 1 h, (d) 1.5 h, and (e) 2 h of ST in 1.0×10^{-9} M aqueous solution of 4MPy. Traces b−e of the absorption spectra have been scaled using uniform scale factor ×5 for visual clarity.

AuNCs show a single absorption maximum peak at ∼534 nm. This band is ascribed to bulk-like surface plasmon resonance (BL-SPR) and had been extensively reported elsewhere.[45,46] The electronic absorption spectrum of the APS is shown in Figure 1, trace b. The spectrum is marked by the decrease in intensity of the BL-SPR band at ∼542 nm along with the appearance of an intense broad maximum at ∼692 nm in the low energy window. The low energy band at ∼692 nm is attributed to the surface-like surface plasmon resonance (SL-SPR) and is known to arise due to dipole−dipole interaction of the aggregated AuNPs on the bilayer LB film matrix of SA.[45−47] The optical signature of this low energy band in the UV−vis electronic absorption spectrum primarily illustrates the existence of gap-plasmonic domains of gold nanoparticles which in turn is known to promote the generation of "hot spots" on the APS. These "hot spots" are recognized to be the special locations on the substrate where the electric fields are strongly localized and the probe molecules trapped within those spots exhibit colossal SERS enhancements.[45,48] However, such conjecture needs to be correlated with the morphology of the substrate from the FESEM and AFM images.

3.2. Characterization of the Bilayer LB Film of SA and APS. The FESEM and AFM images of the bilayer LB film of SA and APS are shown in Figures S2 and S3, respectively, and their morphological features are discussed under section S2 of the Supporting Information. To gain precise information about the elemental composition of APS and to unveil the chemical state and bonding configuration of Au with SA, XPS analyses have been performed. As XPS is a surface sensitive technique and normally probes to a depth of ∼10 nm, we believe for the LB film substrates this technique may be reckoned to be the

https://doi.org/10.1021/acsomega.1c07321
ACS Omega 2022, 7, 27818−27830

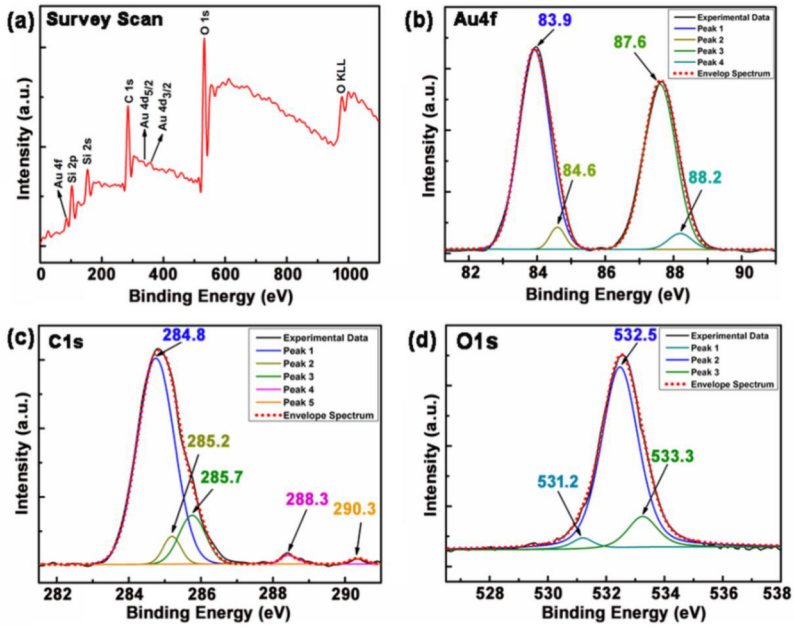

Figure 2. (a) The XPS survey scan of the APS. Narrow scan XPS spectra of the APS in the binding energy windows that represent (b) Au 4f, (c) C 1s, and (d) O 1s regions.

method of choice for such characterizations. The wide range survey scan XPS spectrum of the APS is shown in Figure 2a. A full survey scan spectrum shows the presence of prominent peak characteristic of Au 4f, Si 2p, Si 2s C 1s, Au 4d, and O 1s elements along with Auger peaks O KLL in the order of increasing binding energy (BE) associated with gradual stepwise increase in background. The XPS survey scan thus primarily confirms the presence of carbon (C), oxygen (O), and gold (Au) atoms in the APS. The presence of Si in the bare glass slide upon which the bilayer LB film of SA has been deposited is marked by the appearance of Si 2p and Si 2s peaks. The atomic percentages of Au^0 and Au^+ in the substrates have been specifically estimated using the relation[49]

$$C_i = \left\{ \frac{I_i/X_i}{\sum_j (I_j/X_j)} \right\} \times 100\% \quad (4)$$

where $i,j = Au^0, Au^+$. In eq 4, I_i represents the intensity of the Au^0 and Au^+ peaks while $\sum_j I_j$ depicts the summation of intensities contributing from Au^0 and Au^+ peaks in the XPS spectrum. The intensities I_i and I_j have been enumerated from the estimation of the areas under the respective XPS peaks. The atomic sensitivity factor is represented by X_i, X_j which for the Au 4f peak is considered to be 6.250.[49]

High resolution narrow scan XPS spectra exhibiting in the BE windows of Au 4f, C 1s, and O 1s peaks are shown in Figure 2b–d, respectively. The XPS spectrum in the BE of the Au 4f region has been closely monitored and is shown in Figure 2b. Distinct doublets at ∼83.9 and 87.6 eV with characteristic energy separation (ΔE) ≈ 3.66 eV are observed for the Au 4f peak. Deconvolution of the doublet peaks marks the appearance of two pairs of bands centered at ∼83.9, 84.7 eV and 87.6, 88.3 eV owed to $Au^0 4f_{7/2}$, $Au^+ 4f_{7/2}$, and $Au^0 4f_{5/2}$, $Au^+ 4f_{7/2}$, respectively. These results primarily signify the presence of both the neutral Au^0 atoms and positively charged Au^+ ions on the surface of AuNPs that remain entrapped in the bilayer LB film matrix of SA. However, intensity ratios of the deconvoluted doublet XPS peaks ($IAu^0 4f_{7/2}/IAu^+ 4f_{7/2}$ = 12.57; $IAu^0 4f_{5/2}/ IAu^+ 4f_{7/2}$ = 7.78) imply the preponderance of neutral Au^0 atoms (∼81.57%), albeit the explicit presence of positively charged Au^+ ions (∼18.43%) on the APS cannot be neglected.

The narrow scan XPS spectrum in the C 1s region (Figure 2c) is characterized by an intense and well resolved peak at ∼284.85 eV together with weak but prominent bands peaked at ∼288.3 and 290.3 eV. Upon deconvolution of the experimental data, three peaks appear at ∼284.8, 285.2, and 285.7 eV, while the other two peaks in the higher BE region retain their peak positions at ∼288.3 and 290.3 eV as were recorded in the unconvoluted spectrum. The most prominent peak at ∼284.8 eV originates from the C−C and C−H groups, representing the long aliphatic chain of SA,[50] while the relatively weaker peak at 285.2 eV is attributed to the carbon atoms that are located near the carboxylic group.[51] The peak at 285.7 eV corresponds to the BE associated with the C−O group of SA.[52,53] A weak but distinct peak at ∼288.3 eV is owed to Au-COO^-,[50,54] while the XPS signal at 290.3 eV suggests the presence of a COOH group nonbonded to the AuNPs.[50] A high resolution narrow surface scan in the BE window of C 1s not only justifies the presence of SA but also may point toward probable interaction of its carboxylate group (which remain exposed to air in the bilayer LB film of SA deposited through a Y-type deposition technique) with the Au^+ ions. This interaction in turn may promote the possible entrapment of AuNPs in the bilayer LB film matrix of SA.

Considerable attention may also be drawn from the narrow scan XPS spectrum representing the O 1s signal in the BE window spanning the range of 526.5 to 538 eV. The spectrum is shown in Figure 2d. Deconvolution of the O 1s peak exhibits three bands peaked at 531.2, 532.5, and 533.3 eV. Two weak peaks at ∼531.2 and 533.3 eV may be ascribed to the BEs associated with Au−O and C═O bonds of the carbonyl group, respectively,[55,56] while the most intense peak at 532.5 eV is owed to the C−O bond. These results further indicate the

https://doi.org/10.1021/acsomega.1c07321
ACS Omega 2022, 7, 27818−27830

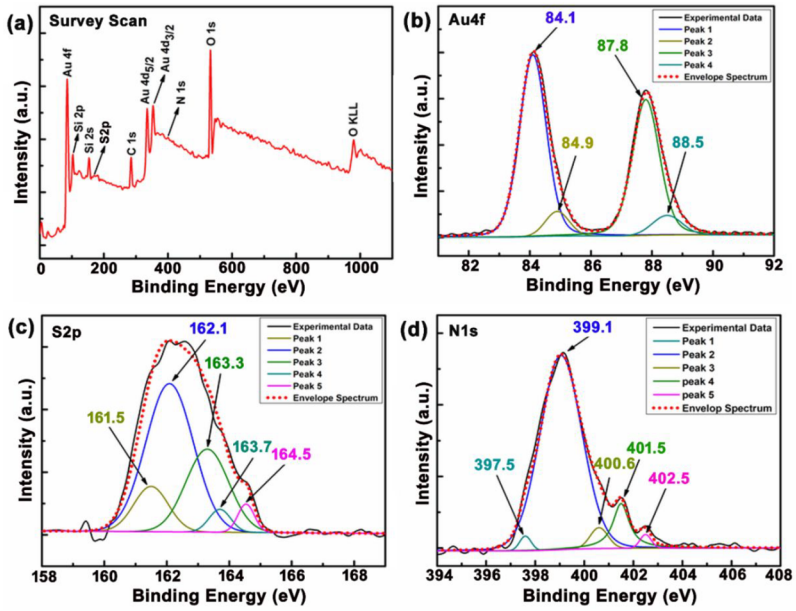

Figure 3. (a) The XPS survey scan of the M-APS so obtained after 2 h of ST. Narrow scan XPS spectra of the M-APS so obtained after 2 h of ST in the binding energy windows that represent (b) Au 4f, (c) S 2p, and (d) N 1s regions.

presence of SA in the LB film substrate and their interaction with AuNPs in agreement with our earlier conjecture.

3.3. Adsorption of the Probe 4MPy Molecule on the APS. An aqueous solution at ∼1.0×10^{-9} M (pH ∼ 7) of the probe 4MPy molecule is soaked on the APSs for 1, 1.5, and 2 h of soaking times (STs). The as-prepared substrate so obtained upon soaking in the solution of the probe 4Mpy molecules will henceforth be designated as the "modified-as prepared substrate (M-APS)" to distinguish it from the APS so fabricated from LB and self-assembly techniques without any adsorption of the probe molecules. The delays in the various STs may allow the probe molecules to penetrate deep into the substrate through gradual diffusion. The UV−vis electronic absorption spectral features of the M-APS substrates so obtained after soaking them in 4Mpy solution for 1, 1.5, and 2 h have been depicted under section S3 of the Supporting Information.

3.4. Characterization of the M-APSs. The FESEM and AFM images of the M-APSs after soaking in aqueous solution of ∼1.0×10^{-9} M 4MPy over various STs are shown in Figures S4 and S5, respectively, and their morphological features are presented under section S4 of the Supporting Information. To understand the adsorption of the 4Mpy molecule on M-APS so obtained after 2 h of ST, the XPS analyses have been performed. The corresponding spectra are shown in Figure 3. The wide range survey scan XPS spectrum for the M-APS (Figure 3a) is markedly different in contrast to the APS substrate as discussed earlier (Figure 2a; *vide supra*). Prominent distinctions are noticed for the Au 4f, Au $4d_{5/2}$, and Au $4d_{3/2}$ XPS peak intensities, which appear as weak signals for the APS. The pronounced increase in intensities of these bands, together with small but definite peak shifts toward higher BE in the XPS spectrum of the M-APS substrate in comparison to that of APS, may signify considerable interaction of 4Mpy with Au. Moreover, the deconvoluted high resolution narrow scan XPS spectrum in the BE window of the Au 4f peak (Figure 3b) further suggests the existence of neutral Au^0 atoms (∼83.52%) in the M-APS, although the presence of Au^+ ions (∼16.48%) on the substrate cannot be ignored. Another contrasting feature that is noticed in the survey scan spectrum of M-APS is the presence of S 2p and N 1s XPS peaks. These peaks are not observed in APS, thereby indicating their origin to be explicitly owed to the probe 4MPy molecule that gets adsorbed in the M-APS.

Close observation may be drawn from the narrow scan XPS spectrum covering the S 2p BE window ranging from 158 to 169 eV (Figure 3c). The narrow scan XPS signal in the S 2p region shows broad spectral signature, distinctively dissimilar to that reported for the free 4MPy molecule in the same BE window.[52] This spectral feature not only just suggests the interaction of 4Mpy with the M-APS but also may signify different chemical states of the sulfur atom.[57] Subsequent deconvolution results in five probable peaks centered at ∼161.5, 162.1, 163.3, 163.7, and 164.5 eV. The peaks at ∼161.5 and 164.5 eV are characteristic of the S $2p_{3/2}$ level, while the peak at 163.7 eV is known to originate from the S $2p_{1/2}$ level of the sulfur atom.[58] The other two peaks at∼ 162.1 and 163.3 eV are owed to $2p_{3/2}$ and $2p_{1/2}$ levels of sulfur, respectively, and their relative intensity ratio ∼2:1 may presage the existence of the thiolate form of the molecule.[59,60] The presence of S^- in the thiolate form of 4Mpy may be involved in the adsorption process with the Au atoms of the AuNPs that remain embedded on the substrate. This conjecture is further substantiated by the absence of any S 2p peak at the higher BE beyond 167 eV, primarily suggesting that the sulfur atom of the 4MPy molecule has not probably been oxidized.[57]

The high resolution XPS spectrum in the N 1s peak region has been recorded and is shown in Figure 3d. The N 1s spectrum has been deconvoluted into five peaks. Among them, the peak centered at ∼397.5 eV is attributed to the BE of the C−N bond associated with the 4MPy molecule.[60] The other deconvoluted peaks at ∼399.1 and at 400.6 and 401.5 eV are reported to emanate from the 4MPyD and 4MPyH forms of the 4-MPy molecule, respectively.[59] Interestingly, a weak but prominent band which appears in a relatively higher BE and

https://doi.org/10.1021/acsomega.1c07321
ACS Omega 2022, 7, 27818−27830

peaked at ∼402.5 eV is ascribed to the oxidized N atom of the 4MPyD form of the 4Mpy molecule.[61]

The above XPS analyses thus collectively suggest the presence of both the 4MPyH and 4MPyD thiolate forms of the 4MPy molecule that remain adsorbed on the M-APS. No evidence presaging the oxidation of the sulfur atom and the presence of the thiolate S^- form together with the presence of the N 1s peak at ∼402.5 eV may signify the adsorption of the 4MPyH and 4MPyD thiolate forms of the 4MPy molecule with the M-APS substrate via the sulfur atom leaving the nitrogen atom free to oxidize.[58,59] Moreover, the complex and broad features in the narrow scan XPS spectra of M-APS in the S 2p and N 1s peak regions (Figure 3c and d) so obtained after 2 h of ST may indeed signify degradation of 4Mpy molecules upon adsorption on the AuNPs embedded in the bilayer LB film matrix of SA.[62,63] However, the conjecture is further strengthened from the SERS spectra of the M-APS substrate and is depicted in the following section.

3.5. SERS spectra of M-APS. The SERS spectra from the M-APS so obtained after soaking in 1.0×10^{-9} M aqueous solution (pH ∼ 7) of 4MPy molecules for 1, 1.5, and 2 h of STs are shown in Figure 4a,b,c, respectively. The spectra are

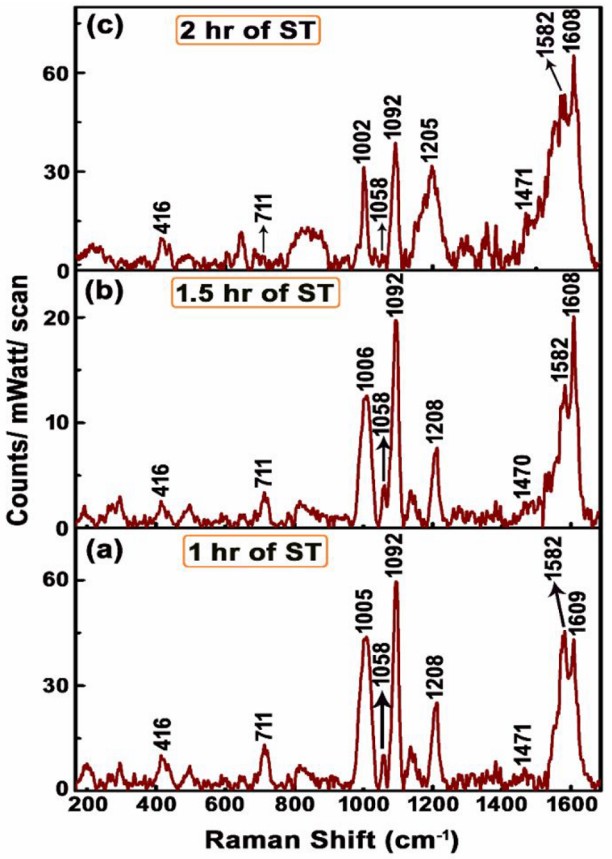

Figure 4. SERS spectra of 1.0×10^{-9} M aqueous solution of 4MPy molecule adsorbed on the M-APSs over various STs (λ_{ex} = 632.8 nm).

marked by distinct vibrational signatures ∼416, 711, 1005, 1058, 1092, 1208, 1582, and 1609 cm^{-1}, characteristic of the 4MPy molecules.[37−39] These observations clearly indicate appreciable efficacies of all of the M-APSs as good SERS sensing platforms. In order to establish the spectral reproducibility, the relative standard deviation (RSD) of the SERS spectra from the M-APS after 2 h of ST has been evaluated. Figure S6 in the Supporting Information shows the SERS spectra of 1.0×10^{-9} M 4MPy molecules so attained after interrogating the laser spot on 10 random regions of the M-APS. The calculated RSD values of the well resolved marker bands of 4-MPy centered at ∼1002, 1092, 1582, and 1608 cm^{-1} are 11.88%, 9.19%, 11.19%, and 12.34%, respectively. The estimated RSD value of <13% marks the reproducibility of the as prepared M-APS. However, changes in relative intensity of the SERS spectra as shown in Figure 4 and S6 from spot to spot may signify partial degradation of the molecule on the surface, most probably due to the large adsorption time adopted. The normal Raman spectrum (NRS) of 4MPy in aqueous medium (pH ∼ 7) at 1 M concentration is also recorded and is shown in Figure S7 (Supporting Information). The NRS spectrum exhibits Raman modes of vibrations centered at around ∼429, 723, 1001, 1053, 1114, 1207, 1487, 1589, and 1621 cm^{-1}, all known to emanate from the protonated and deprotonated thione and the thiol forms of the 4MPy molecule.[37,64−66] Interestingly, appreciable changes in relative intensities are noted for the SERS bands of the 4MPy molecules centered at ∼1005, 1092, 1208, 1582, and 1609 cm^{-1} depending upon the STs of the probe molecule on the M-APSs. The enhanced Raman bands at ∼1005, 1092, 1609, and 1582 cm^{-1} in the SERS spectra are ascribed to A_1 and B_2 irreducible representations, respectively.[38,40,41,67] These changes may primarily signify the presence of both the 4MpyH and 4MpyD thione forms of the 4Mpy molecule, which are known to coexist in different proportions under similar experimental conditions and have been extensively reported in our earlier publication.[39] Alternatively, the selective enhancements of Raman bands in the SERS spectra belonging to A_1 and B_2 irreducible representations (*vide supra*) may be accounted from the CT interaction between the probe molecule and the AuNP systems. Since the concentration (∼1.0×10^{-9} M) and pH of the adsorbate 4Mpy molecules in aqueous solution remain the same, we believe the variations in the intensities of the enhanced bands in the SERS spectra may be due to CT interactions between AuNPs and the existing 4MPyH and 4MPyD forms of the 4Mpy molecule in the surface adsorbed state. The prevalence of CT interaction is further substantiated by appreciable downshifts of SERS bands at around ∼711 and 1092 cm^{-1}, whose NRS counterparts are recorded at 723 and 1114 cm^{-1}, respectively. The bands at ∼711 and 1092 cm^{-1} are assigned to mixed υ(C−S) stretching, in-plane β(C−C) bending (ν_6), and the ring breathing mode [$12a_1$] coupled with υ(C−S) stretching vibrations, respectively.[39,40] Furthermore, remarkable downshifts of both of these bands may signify plausible interaction of the 4MPy molecule with the AuNPs through lone pair electrons of the sulfur (S) atom. This conjecture is in line with the observation as predicted from the XPS studies (*vide supra*). The rationale behind the CT interaction may be further extended from the intensity reversals between the pair of bands ∼1582 and 1608 cm^{-1} in the SERS spectra of the 4Mpy molecule (Figure 4a−c) belonging to B_2 and A_1 irreducible representations, respectively.[41,68] The intensity reversals between these pairs of bands owing to B_2 and A_1 irreducible representations are attributed to CT interactions driven by intensity borrowing from the strongly allowed molecular transition of the 4MPy molecule.[68] Close inspection of the SERS spectra further reveals unusual broadening and change in intensity of the enhanced Raman band at ∼1608 cm^{-1} with ST. The unusual broadening and change in intensity of the enhanced Raman bands may be

https://doi.org/10.1021/acsomega.1c07321
ACS Omega 2022, 7, 27818−27830

attributed to partial degradation of the 4Mpy molecule upon adsorption on the AuNPs that remains embedded in the bilayer LB film matrix of SA.[62,63] This conjecture is further corroborated by the complex and broad features in the narrow scan XPS spectra in the binding energy window linked with the S 2p and N 1s peaks (Figure 3c and d) of the M-APSs.[62,63] To gain deeper insights into the adsorption behavior of 4Mpy with M-APS, BO-OF-MD and DFT calculations have been further explored with the aid of molecule−metal adatoms models.[59,69−71] The results of the pre- referred calculations are depicted in the following section.

3.6. Born−Oppenheimer Molecular Dynamics and DFT Calculations on the Molecule- Au cluster Models.

To corroborate the CT effect of SERS, as evinced from the experimental observations (*vide supra*), the adatom or small metal cluster models have been adopted to understand the Au-4Mpy interactions from the DFT calculations.[59,69−71] These adatom or adcluster models ensure the importance of specific surface-active site/sites on the metal nanoparticles that are explicitly involved in the chemisorption processes with the external probe molecules.[19,72] The surface active adatoms or adclusters contain single or few metal atoms or ions and remain relatively isolated from the bulk metal.[73] Recent reports suggest that pragmatic applications of such models have the real power to reproduce the experimentally observed SERS spectra of various metal−molecule systems in terms of both their vibrational frequencies and their relative intensities.[8−11,16−21,50,74,75]

However, to envisage a reliable model of the metal adcluster that can get involved in the binding processes with both the existing 4MpyH and 4MpyD forms of the 4MPy molecule on the "M-APSs", the partial radial distribution function $g(r)$ between the Au and the sulfur (S1) and nitrogen (N9) atoms of the probe molecule have been estimated from BO-OF-MD simulations. The partial radial distribution function not only provides a firm basis to enumerate the composition of atom/atoms in the Au adcluster but also helps in understanding their interactions with the specific atom/atoms of the probe molecule, useful for the ensuing DFT calculations. Figure 5a and b show the variation of $g(r)$ as a function of radial distances between the S1−Au for 4MpyH and the N9−Au and S1−Au atoms for 4MpyD forms of the molecule, respectively. The radial distributions show one prominent peak (Figure 5a), centered at ∼2.53 Å, signifying the average distance between the S1 of 4MpyH and the Au atoms of the adcluster. Such a close distance of ∼2.53 Å between S1 and Au atoms may primarily indicate probable involvement of the sulfur (S1) atom of the 4MpyH molecule in the adsorption process with AuNPs. Interestingly, the variations of $g_{S1-Au}(r)$ and $g_{N9-Au}(r)$ as a function of distance for the 4MpyD molecule, as shown in Figure 5b, divulge some interesting observations. While $g_{S1-Au}(r)$ exhibits the most prominent peak at a distance of ∼2.35 Å, the first prominent maximum of $g_{N9-Au}(r)$ however appears at a comparatively larger distance of ∼4.02 Å. These results may signify the involvement of a sulfur (S1) instead of a nitrogen (N9) atom, even in the adsorption of 4MpyD forms of the probe molecule with AuNPs, as being suggested for its 4MPyH form (vide *supra, cf.* Figure 3). Close inspection of Figure 5a and b shows the appearance of a weak peak at ∼5.2 Å. The appearance of the weak peak may signify the average distance between S1 of 4MpyH/4MpyD and the Au atoms of the adcluster in the second solvation shell of the Au atoms.[76−79] Integrating the areas under the curves represented by the first distinct peak of the $g_{S1-Au}(r)$ plots (Figure 5a and b) for the 4MpyH and 4MpyD forms of the molecule yields the integration numbers ∼2.81 and 2.96, respectively. These results suggest the existence of a maximum of three or minimum of two Au atoms in the first neighboring shell near the sulfur (S1) atom of both the 4MPyH and 4MPyD forms of the 4Mpy molecule. Thus, three or two Au atoms in neutral or in positively charged forms may constitute the Au_n adcluster (n = 3, 2) model to best represent the surface-active site of the AuNPs.

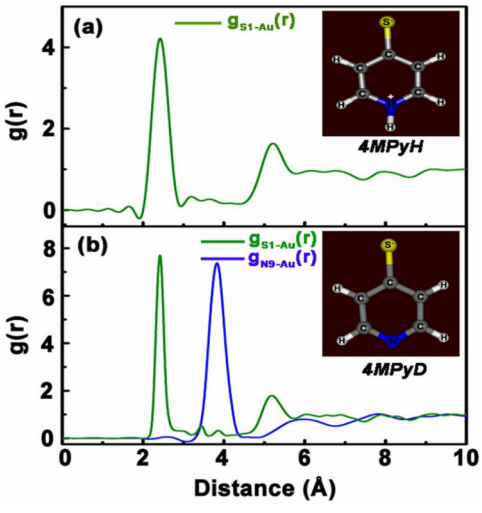

Figure 5. Partial radial distribution function $g(r)$ for (a) 4MpyH and (b) 4MpyD forms of the molecule in the presence of surrounding Au atoms as estimated from BO-OF-MD simulation.

The energy of the Au_3 cluster has been equilibrated over a period of time ranging from 0 to 30 ps (ps) with the aid of the BO-OF-MD calculation. The results are shown as a blue trace in Figure S8a in the Supporting Information. After initial structural flexing and relaxations, the energy of the Au_3 cluster system is noted to be stabilized after 10 ps of the simulation run. The probable structure of the Au_3 cluster evolved at ∼12 ps is shown in the inset of Figure S8a. The frequency distributions showing variations of the r(Au−Au) bond length and ∠Au−Au−Au bond angle as obtained from the corresponding BO-OF-MD trajectory are shown in Figure S8b and c, respectively. The weighted average values of the r(Au−Au) bond length and ∠Au−Au−Au bond angle for the Au_3 cluster are estimated to be ∼2.595 Å and 136°, respectively. The initial structural parameters of the Au_3 cluster, as obtained from the BO-OF-MD simulation, have been fed for further geometry optimization using DFT calculations with the B3LYP/LANL2DZ level of theory. The optimized structural parameters of the Au_3 cluster as estimated from BO-OF-MD and DFT calculations are shown in Table S1 in the Supporting Information. Figure 6 shows different adsorptive stances of neutral (Au_3^0) as well as charged $Au^+Au^0Au^0$, $Au^+Au^+Au^0$, and $Au^+Au^+Au^+$ cluster systems with 4MpyH and 4MpyD forms of the probe molecule. The inclusion of neutral and charged Au atoms in various Au_3 adcluster models stem from the XPS spectra of M-APS that marks the presence of both neutral (Au^0) and charged Au^+ ions as discussed earlier (*cf.* section 3.4). Significantly enough, among the estimated SCF energies of the probable Au_3-molecule adatom models, the 4MPyH−$Au^0Au^0Au^0$ and

https://doi.org/10.1021/acsomega.1c07321
ACS Omega 2022, 7, 27818−27830

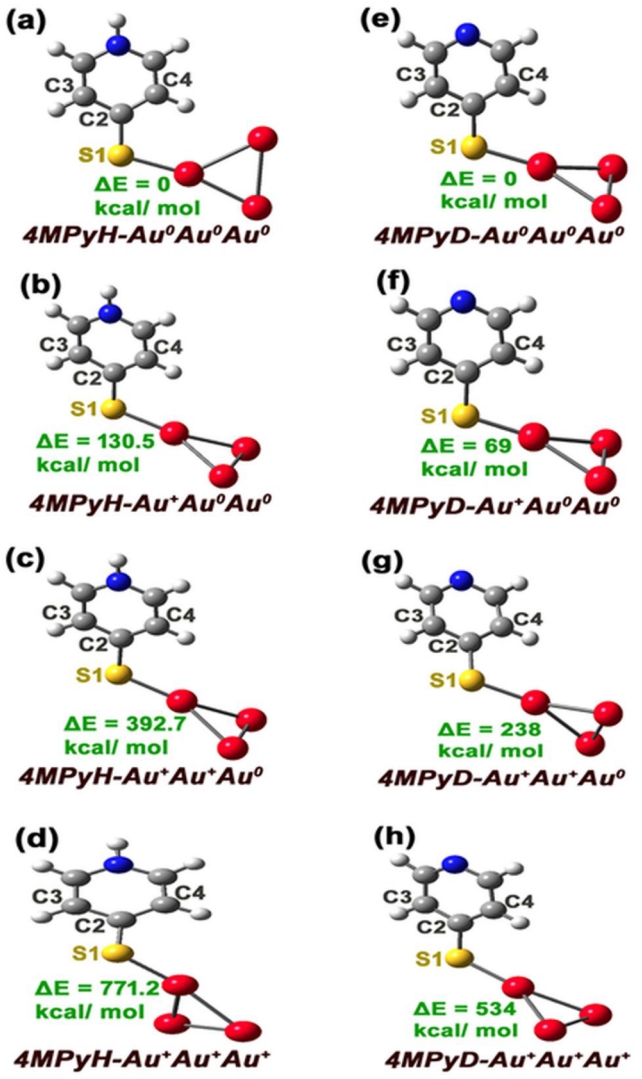

Figure 6. Optimized geometries of the model complexes of (a) 4MPyH−$Au^0Au^0Au^0$, (b) 4MPyH−$Au^+Au^0Au^0$, (c) 4MPyH−$Au^+Au^+Au^0$, (d) 4MPyH−$Au^+Au^+Au^+$, (e) 4MPyD−$Au^0Au^0Au^0$, (f) 4MPyD−$Au^+Au^0Au^0$, (g) 4MPyD−$Au^+Au^+Au^0$, and (h) 4MPyD−$Au^+Au^+Au^+$ adclusters so obtained from DFT calculations with the B3LYP/6-31++g(d,p) [for C, H, N and S]/LANL2DZ (for Au atoms) level of theory.

4MpyD−$Au^0Au^0Au^0$ surface complexes are found to be thermodynamically most stable. These results are in line with the XPS studies that smear the presence of Au^0 atoms in abundance on the M-APS (*vide ante*; *cf.* section 3.4). Figure S9 in the Supporting Information shows the theoretically simulated Raman spectra of 4MPyH−$Au^0Au^0Au^0$, 4MPyH−$Au^+Au^0Au^0$, 4MPyH−$Au^+Au^+Au^+$, 4MpyD−$Au^0Au^0Au^0$, 4MpyD−$Au^+Au^0Au^0$, 4MpyD−$Au^+Au^+Au^+$, and their corresponding mixed forms. Interestingly, neither of the calculations can reproduce the experimentally recorded SERS spectra, although among them the 4MPyH/4MPyD−$Au^0Au^0Au^0$ adcluster models are estimated to be most stable from theromdynamical considerations. On the contrary, the Raman spectra of the mixed, 4MpyH−$Au^+Au^+Au^0$ (IA), and 4MpyD−$Au^+Au^+Au^0$ (IIA) forms, as estimated from the DFT calculations, are shown in Figure 7, which is in close agreement with the experimentally observed SERS spectra of the molecule. The calculated vibrational frequencies of 4MpyH−

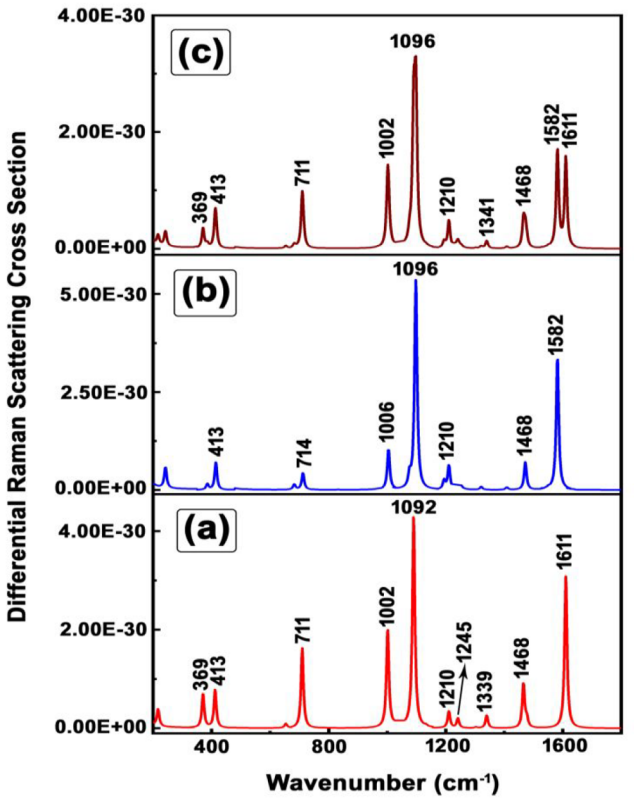

Figure 7. Theoretically simulated Raman spectra of (a) 4MPyH−$Au^+Au^+Au^0$ (IA), (b) 4MPyD−$Au^+Au^+Au^0$ (IIA), and (c) mixed form $Au^+Au^+Au^0$ (IA, IIA) adcluster models as estimated from the B3LYP/6-31++g(d,p) [for C, H, N, and S]/LANL2DZ (for Au atoms) level of theory.

$Au^+Au^+Au^0$ and 4MpyD−$Au^+Au^+Au^0$ model complexes along with the experimentally observed SERS bands at various STs are shown in Table S2 in the Supporting Information along with some of their tentative assignments.

The optimized geometrical parameters of some selected bond lengths and bond angles of 4MpyH−$Au^+Au^+Au^0$, 4MpyD−$Au^+Au^+Au^0$ model complexes as estimated from the DFT calculations are shown in Table S3 in the Supporting Information. Moreover, the other possible interaction configuration of 4MPyH/4MPyD−Au_3 may involve binding of the sulfur atom with the two gold atoms of the Au_3 adcluster. The DFT calculations have also been performed for the newly proposed 4MpyH−$Au^+Au^+Au^0$ (IB), 4MpyD−$Au^+Au^+Au^0$ (IIB) adcluster models. The optimized geometries of 4MpyH−$Au^+Au^+Au^0$ and 4MpyD−$Au^+Au^+Au^0$ adcluster models so obtained from DFT calculations are shown in Figure S10 in the Supporting Information. Figure S11 in the Supporting Information shows theoretically simulated Raman spectra of the newly proposed 4MpyH−$Au^+Au^+Au^0$ and 4MpyD−$Au^+Au^+Au^0$ adcluster models and their corresponding mixed forms. However, from Figure S11 in the Supporting Information, it is clearly seen that the theoretically simulated spectra for newly proposed adcluster models fail to reproduce the experimentally recorded SERS spectra (*vide supra, cf.* Figure 4) in terms of both band positions and intensities.

Interesting observations may be drawn from the results of WT theory, which can estimate the fluctuations of the Au−S1 bond length as a function of time. The temporal variations of the Au−S1 bond length for 4MPyH−$Au^+Au^+Au^0$ and

https://doi.org/10.1021/acsomega.1c07321
ACS Omega 2022, 7, 27818−27830

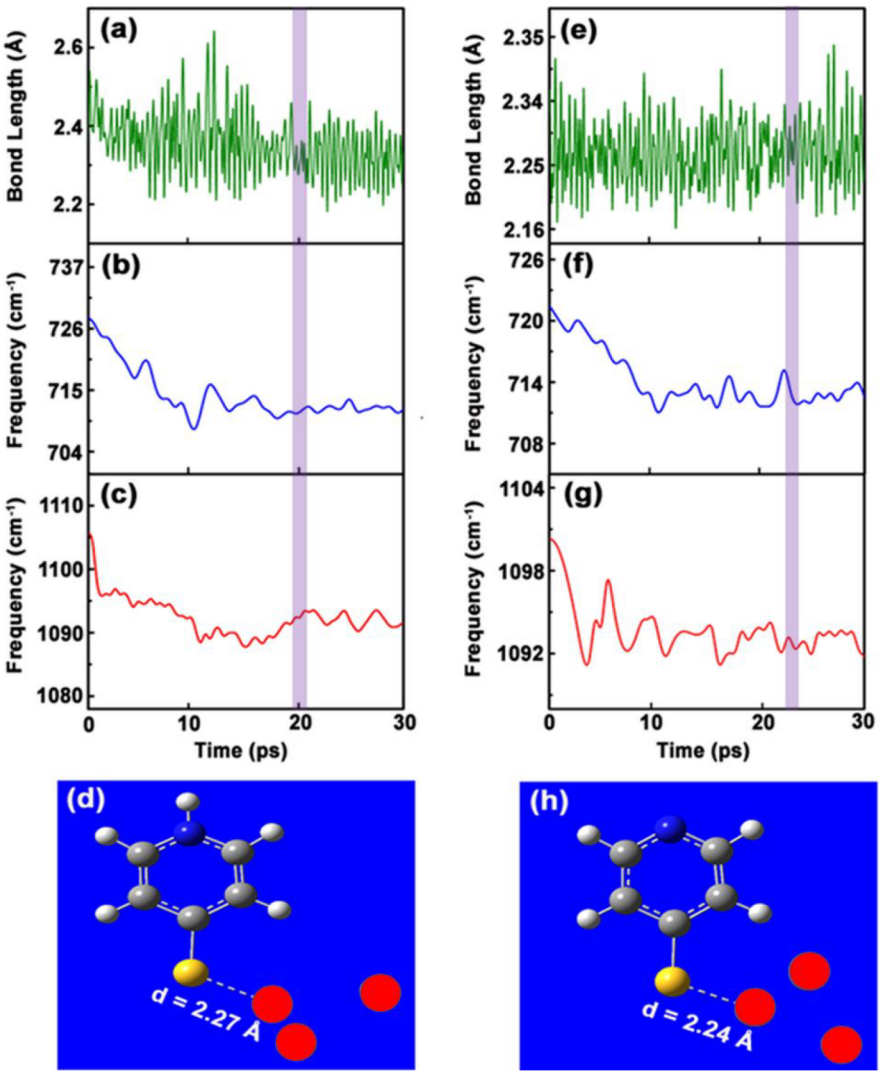

Figure 8. Time evolution of Au−S1bond length of (a) 4MPyH−$Au^+Au^+Au^0$ and (e) 4MPyH−$Au^+Au^+Au^0$ clusters as obtained from BO-OF-MD simulations. Time resolved band stretching frequencies of the C2−S1 bond of (b,c) 4MPyH−$Au^+Au^+Au^0$ and (f,g) 4MPyD−$Au^+Au^+Au^0$ clusters as obtained from wavelet transform theory. Discrete snapshots of the BO-OF-MD simulations for (d) 4MpyH—$Au^+Au^+Au^0$ and (h) 4MpyD—$Au^+Au^+Au^0$ models captured on 20 and 23 ps time scales, respectively, at T = 300 K.

4MpyD−$Au^+Au^+Au^0$ model complexes on the picosecond time scale are shown in Figure 8a,e. The VDOS of the ν_6 [β(C−C)/ν(C−S)] and ν_{12} [trigonal ring-breathing with C═S deformation] normal mode for 4MpyH−$Au^+Au^+Au^0$ and 4MpyD−$Au^+Au^+Au^0$ model complexes have also been estimated from WT theory and are also shown in Figure 8b,c and f,g, respectively. From Figure 8a−c and e−g, it is clearly seen that the vibrational frequencies of the normal modes ν_6 and ν_{12} are significantly downshifted from ∼728 to 707 cm^{-1} (∼721 to 710 cm^{-1}) and ∼1105 to 1087 cm^{-1} (∼1100 to 1091 cm^{-1}) as the Au atom approaches in the close proximity of the S1 atom for the 4MPyH (4MPyD) forms of the 4MPy molecule. These results collectively suggest the probable adsorption of the S1 atom with Au not only for the 4MPyH and 4MPyD but for the mixed form of the 4MPy molecule as well. The time-resolved vibrational frequencies, as estimated from VDOS, further corroborate the experimentally recorded SERS spectra of the 4MPy molecule, which show significant red shifts of the enhanced vibrational frequencies at ∼711 and 1092 cm^{-1} compared to its NRS counterpart at ∼721 and 1114 cm^{-1}, respectively (*vide supra. cf.* Figure 4). The discrete snapshots of the 4MPyH—$Au^+Au^+Au^0$ and 4MPyD—$Au^+Au^+Au^0$ model systems captured on the 20 and 23 ps time scales of the simulation run are shown in Figure 8d and h, respectively. Interestingly, from BO-OF-MD simulations, the Au—S1 distances for 4MpyH—$Au^+Au^+Au^0$/4MPyD—$Au^+Au^+Au^0$ model systems are estimated to be 2.27(±0.017)/2.24(±0.014) Å, in close harmony with that estimated from DFT calculations 2.36/2.37 Å for the most probable 4MpyH−$Au^+Au^+Au^0$/4MPyD−$Au^+Au^+Au^0$ adcluster models.

The electron densities that are harbored in the 4MPyH and 4MPyD molecules and in the $Au^+Au^+Au^0$ metal cluster models are shown in Figure 9a, b, and c, respectively. From Figure 9a and b, it is clearly seen that the electron densities are strongly localized on C, N, and S atoms of the respective aromatic rings of the 4MPyH and 4MPyD molecules. The electron densities for the $Au^+Au^+Au^0$ clusters are however confined on the Au atoms (Figure 9c). Figure 9d and e show the EDDs that are perceived in 4MPyH−$Au^+Au^+Au^0$ and 4MPyD−$Au^+Au^+Au^0$

https://doi.org/10.1021/acsomega.1c07321
ACS Omega 2022, 7, 27818−27830

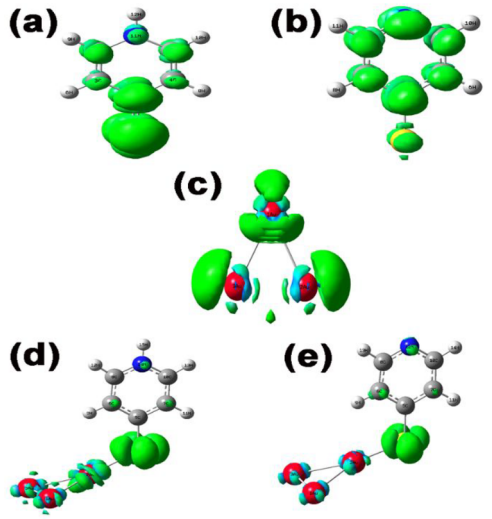

Figure 9. Electron density of (a) 4MPyH, (b) 4MPyD, and (c) $Au^+Au^+Au^0$ metal and electronic density differences of (d) 4MPyH−$Au^+Au^+Au^0$ and (e) 4MPyD−$Au^+Au^+Au^0$ adclusters as estimated from the B3LYP/6-31++g(d,p) [for C, H, N, and S]/LANL2DZ (for Au atoms) level of theory (isosurface value = 0.005 a.u).

molecule-Au cluster models, respectively. Figure 9d and e clearly reveal depletion of charge clouds on the respective aromatic rings of 4MPyH and 4MPyD molecules and accumulation of electron density clouds on their respective S atoms and on the Au atoms of the adclusters. These observations may signify appreciable shifts of electron clouds from the aromatic rings of the molecule to the Au metal atoms, thereby suggesting molecule → metal CT interaction. The molecule → metal CT contribution to SERS may be envisaged from the broadening and appreciable downshifts of the enhanced Raman bands centered at ∼711 and 1092 cm^{-1} (*vide supra, cf.* Figure 4) whose NRS counterparts are recorded at 723 and 1114 cm^{-1} [*vide supra, cf.* Figure S7 (Supporting Information)], respectively.[80] Moreover, selective enhancements and considerable shifts of the Raman bands at ∼1582 and 1608 cm^{-1} in the SERS spectra further signify the involvement of CT interaction in the overall enhancement of the Raman bands of the 4MPy molecule.[68] To quantify the molecule → metal CT interaction, the charge transfer distance or the descriptor (D_{CT}) has been estimated. A partial charge (namely Mulliken's) analysis has been adopted to calculate D_{CT}, whose in-depth analysis has been reported elsewhere.[81] The charge transfer distance (D_{CT}) and the amount of charge transfer have been estimated to be ∼2.41 Å and 0.91 |e| and 2.39 Å and 0.79 |e| for 4MpyH−$Au^+Au^+Au^0$ and 4MpyD−$Au^+Au^+Au^0$ model complexes, respectively.

4. CONCLUSION

Adsorption of 4Mpy molecules with AuNPs embedded in the LB film matrix of stearic acid has been elucidated in detail from SERS and XPS studies. The as-fabricated LB film substrate was soaked in the aqueous solution (∼1.0×10^{-9} M) of 4MPy over various soaking times ranging from 1 to 2 h. All of the MAPSs proved to be good SERS sensing platforms and can detect the analyte 4MPy molecules at a trace concentration (∼1.0×10^{-9} M). The XPS study not only signifies the adsorption of 4Mpy molecules with AuNPs via a sulfur atom but also suggests partial degradation of the analyte molecule upon adsorption. This result is further corroborated from the SERS spectral profile, which shows unusual broadening of the enhanced Raman bands of the molecule. The experimental observations are aided by BO-OF-MD, time-resolved WT theory, and DFT calculations based on analyte molecule−metal adcluster models. The CT contribution to the overall enhanced Raman bands of the 4MPy molecule has also been envisaged from electron density difference calculations, and the corresponding CT distance has been estimated from the descriptor (D_{CT}).

■ ASSOCIATED CONTENT

Supporting Information

The Supporting Information is available free of charge at https://pubs.acs.org/doi/10.1021/acsomega.1c07321.

Pressure−area isotherm plot of stearic acid; morphological characterization of the bilayer LB film of SA and APS; FESEM images of (a) bare quartz slide, (b) SA bilayer LB film, and (c) AuNPs self-assembled on the LB film matrix of SA; 2D and 3D AFM images of the APS; UV−vis absorption spectra of the M-APSs; morphological characterization of the M-APSs; SERS spectra of 1.0×10^{-9} M 4MPy at pH ∼ 7, recorded from 10 distinct spots of the M-APS so obtained after 2 h of ST; background corrected normal Raman spectrum (NRS) of 1 M 4MPy in aqueous solution (λ_{ex} = 632.8 nm); (a) energy vs time plot of Au_3 cluster over 30 ps time scale as obtained from the BO-OF-MD calculations; statistical distributions of (b) Au−Au bond lengths and (c) Au−Au−Au bond angles; optimized structural parameters of the Au_3 cluster as obtained from BO-OF-MD and DFT calculations with the B3LYP/Lanl2DZ level of theory; theoretically simulated Raman spectra of (i, a) 4MPyH−$Au^0Au^0Au^0$, (b) 4MPyD−$Au^0Au^0Au^0$, and (c) mixed $Au^0Au^0Au^0$ adclusters; (ii, a) 4MPyH−$Au^+Au^0Au^0$, (b) 4MPyD−$Au^+Au^0Au^0$, and (c) mixed $Au^+Au^0Au^0$ adclusters; (iii, a) 4MPyH−$Au^+Au^+Au^+$, (b) 4MPyD−$Au^+Au^+Au^+$, and (c) mixed $Au^+Au^+Au^+$ adclusters using the B3LYP/6-31++g(d,p) [for C, H, N, and S]/LANL2DZ (for Au atoms) level of theory; simulated frequencies of 4MPyH−$Au^+Au^+Au^0$ and 4MPyD−$Au^+Au^+Au^0$ complexes compared with the experimentally observed SERS frequencies of 4MPy adsorbed on the Au nanoparticles' surface at different STs along with their tentative assignments; relevant structural parameters of 4MpyH/4MpyD−$Au^+Au^+Au^0$ model complexes as obtained from DFT calculations with the B3LYP/6-31++g(d,p) [for C, H, N, and S]/LANL2DZ (for Au atoms) level of theory; optimized geometries of the model complexes of (a) 4MpyH−$Au^+Au^+Au^0$ and (b) 4MpyD−$Au^+Au^+Au^0$ adclusters so obtained from DFT calculations with the B3LYP/6-31++g(d,p) [for C, H, N, and S]/LANL2DZ (for Au atoms) level of theory; theoretically simulated Raman spectra of (a) 4MPyH−$Au^+Au^+Au^0$, (b) 4MPyD−$Au^+Au^+Au^0$, and (c) mixed form $Au^+Au^+Au^0$ adcluster models as estimated from B3LYP/6-31++g(d,p) [for C, H, N, and S]/LANL2DZ (for Au atoms) level of theory (PDF)

■ AUTHOR INFORMATION

Corresponding Author

Joydeep Chowdhury − *Department of Physics, Jadavpur University, Kolkata 700032, India;* orcid.org/0000-0001-

https://doi.org/10.1021/acsomega.1c07321
ACS Omega 2022, 7, 27818−27830

9952-9956; Email: joydeep72_c@rediffmail.com, joydeep.chowdhury@jadavpuruniversity.in

Authors

Somsubhra Saha − *Department of Physics, Jadavpur University, Kolkata 700032, India*

Bipan Dutta − *Department of Physics, Sammilani Mahavidyalaya, Kolkata 700094, India*

Manash Ghosh − *Department of Spectroscopy, Indian Association for the Cultivation of Science, Kolkata 700032, India*

Complete contact information is available at: https://pubs.acs.org/10.1021/acsomega.1c07321

Author Contributions

‖Equal contributions.

Notes

The authors declare no competing financial interest.

■ ACKNOWLEDGMENTS

Authors express their thanks to the Council of Scientific & Industrial Research (CSIR), Department of Science and Technology (DST, SERB, Govt. of India), and the Department of Higher Education, Science & Technology and Biotechnology (DHESTB, Govt. of West-Bengal), for financial support through research projects [Project Sanction No.: 03(1437)/18/EMR-II, EMR/2017/000901, and 202 (Sanc.)/ST/P/S&T/16G-22/2017)]. The authors would like to thank the Department of Physics, Jadavpur University, for recording the FESEM images and also for providing a departmental computational facility through the DST-FIST program. S.S. would like to thank UGC, Govt. of India, for the Senior Research Fellowship (SRF) through the NFSC fellowship scheme. The authors would like to thank Mr. Uttam Ghara, IIT Kharagpur for recording the XPS spectra.

■ REFERENCES

(1) Fleischmann, M.; Hendra, P. J.; McQuillan, A. J. Raman spectra of pyridine adsorbed at a silver electrode. *Chem. Phys. Lett.* **1974**, *26*, 163−166.

(2) Das, S. K.; Bhattacharya, T. S.; Ghosh, M.; Chowdhury, J. Probing blood plasma samples for the detection of diabetes using SERS aided by PCA and LDA multivariate data analyses. *New. J. Chem.* **2021**, *45*, 2670−2682.

(3) Lee, T.; Kwon, S.; Choi, H.-J.; Lim, H.; Lee, J. Highly Sensitive and Reliable microRNA Detection with a Recyclable Microfluidic Device and an Easily Assembled SERS Substrate. *ACS Omega* **2021**, *6*, 19656−19664.

(4) Yadav, S.; Sadique, M. A.; Ranjan, P.; Kumar, N.; Singhal, A.; Srivastava, A. K.; Khan, R. SERS Based Lateral Flow Immunoassay for Point-of-Care Detection of SARS-CoV-2 in Clinical Samples. *ACS Appl. Bio Mater.* **2021**, *4*, 2974−2995.

(5) Murugesan, B.; Yang, J. Tunable Coffee Ring Formation on Polycarbonate Nanofiber Film for Sensitive SERS Detection of Phenylalanine in Urine. *ACS Omega* **2019**, *4*, 14928−14936.

(6) Pramanik, A.; Gao, Y.; Patibandla, S.; Mitra, D.; McCandless, M. G.; Fassero, L. A.; Gates, K.; Tandon, R.; Chandra Ray, P. The rapid diagnosis and effective inhibition of coronavirus using spike antibody attached gold nanoparticles. *Nanoscale Adv.* **2021**, *3*, 1588−1596.

(7) Yu, Y.; Zeng, P.; Yang, C.; Gong, J.; Liang, R.; Ou, Q.; Zhang, S. Gold-Nanorod-Coated Capillaries for the SERS-Based Detection of Thiram. *ACS Appl. Nanomater.* **2019**, *2*, 598−606.

(8) Grys, D.-B.; de Nijs, B.; Salmon, A. R.; Huang, J.; Wang, W.; Chen, W.-H.; Scherman, O. A.; Baumberg, J. J. Citrate Coordination and Bridging of Gold Nanoparticles: The Role of Gold Adatoms in AuNP Aging. *ACS Nano* **2020**, *14*, 8689−8696.

(9) Muniz-Miranda, M.; Muniz-Miranda, F.; Pedone, A. SERS and DFT investigation on push-pull molecules: 4-Dimethylamino- 4′-nitrostilbene adsorbed on silver colloidal nanoparticles. *Chem. Select* **2018**, *3*, 8698−8702.

(10) Muniz-Miranda, M.; Muniz- Miranda, F.; Caporali, S.; Calisi, N.; Pedone, A. SERS, XPS and DFT investigation on palladium surfaces coated with 2,2′-bipyridine monolayers. *Appl. Surf. Sci.* **2018**, *457*, 98−103.

(11) Tsunoi, A.; Lkhamsuren, G.; Mondarte, E. A. Q.; Asatyas, S.; Oguchi, M.; Noh, J.; Hayashi, T. Improvement of the Thermal Stability of Self-Assembled Monolayers of Isocyanide Derivatives on Gold. *J. Phys. Chem. C* **2019**, *123*, 13681−13686.

(12) Bhamidipati, M.; Lee, G.; Kim, I.; Fabris, L. SERS-Based Quantification of PSMA in Tissue Microarrays Allows Effective Stratification of Patients with Prostate Cancer. *ACS Omega* **2018**, *3*, 16784−16794.

(13) Yang, Y.; Kannisto, E.; Patnaik, S. K.; Reid, M. E.; Li, L.; Wu, Y. Ultrafast Detection of Exosomal RNAs via Cationic Lipoplex Nanoparticles in a Micromixer Biochip for Cancer Diagnosis. *ACS Appl. Nanomater.* **2021**, *4*, 2806−2819.

(14) Wang, H.; Xue, Z.; Wu, Y.; Gilmore, J.; Wang, L.; Fabris, L. Rapid SERS Quantification of Trace Fentanyl Laced in Recreational Drugs with a Portable Raman Module. *Anal. Chem.* **2021**, *93*, 9373−9382.

(15) Moram, S. S. B.; Byram, C.; Shibu, S. N.; Chilukamarri, B. M.; Soma, V. R. Ag/Au Nanoparticle-Loaded Paper-Based Versatile Surface-Enhanced Raman Spectroscopy Substrates for Multiple Explosives Detection. *ACS Omega* **2018**, *3*, 8190−8201.

(16) Dao, D. Q.; Ngo, T. C.; Le, T. T. H.; Trinh, Q. T.; Nguyen, T. L. A.; Huy, B. T.; Tri, N. N.; Trung, N. T.; Nguyen, M. T. SERS Chemical Enhancement of 2,4,5-Trichlorophenoxyacetic Acid Adsorbed on Silver Substrate. *J. Phys. Chem. A* **2021**, *125*, 8529−8541.

(17) Ngo, T. C.; Trinh, Q. T.; Thi Thai An, N.; Tri, N. N.; Trung, N. T.; Truong, D. H.; Huy, B. T.; Nguyen, M. T.; Dao, D. Q. SERS Spectra of the Pesticide Chlorpyrifos Adsorbed on Silver Nano surface: The Ag_{20} Cluster Model. *J. Phys. Chem. C* **2020**, *124*, 21702−21716.

(18) Birke, R. L.; Lombardi, J. R.; Saidi, W. A.; Norman, P. Surface-Enhanced Raman Scattering Due to Charge-Transfer Resonances: A Time-Dependent Density Functional Theory Study of Ag_{13}-4-Mercaptopyridine. *J. Phys. Chem. C* **2016**, *120*, 20721−20735.

(19) Lopez-Tocon, I.; Valdivia, S.; Soto, J.; Otero, J. C.; Muniz-Miranda, F.; Menziani, M. C.; Muniz-Miranda, M. A DFT Approach to the Surface-Enhanced Raman Scattering of 4-Cyanopyridine Adsorbed on Silver Nanoparticles. *Nanomat.* **2019**, *9*, 1211−1222.

(20) Zoppi, A.; Caporali, S.; Muniz-Miranda, F.; Pedone, A.; Muniz-Miranda, M. Adsorption of Trans-Zeatin on Laser-Ablated Gold Nanoparticles for Transport into Plant Cells and Growth Stimulation. *ACS Appl. Nanomater.* **2019**, *2*, 7319−7327.

(21) Wang, R.; Shen, X.-R.; Zhang, M.; Devasenathipathy, R.; Pang, R.; Wu, D.-Y.; Zhang, J.; Ulstrup, J.; Tian, Z.-Q. Adsorption, Chemical Enhancement, and Low-Lying Excited States of p-Methylbenzenethiol on Silver and Gold Nanoparticle Surfaces: A Surface Enhanced Raman Spectroscopy and Density Functional Theory Study. *J. Phys. Chem. C* **2019**, *123*, 23026−23036.

(22) Frens, G. Controlled nucleation for the Regulation of the Particle Size in Monodisperse Gold Suspensions. *Nat. Phys. Sci.* **1973**, *241*, 20−22.

(23) Basu, S.; Ghosh, S. K.; Kundu, S.; Panigrahi, S.; Praharaj, S.; Pande, S.; Jana, S.; Pal, T. Biomolecule induced nanoparticle aggregation: effect of particle size on interparticle coupling. *J. Colloid Interface Sci.* **2007**, *313*, 724−734.

(24) *CPMD*. IBM Corp., 1990−2008; Copyright MPI fur Festkorperforschung Stuttgart, 1997−2001. http://www.cpmd.org.

(25) Kim, B. J.; Bang, J.; Hawker, C. J.; Kramer, E. J. Effect of Areal Chain Density on the Location of Polymer-Modified Gold Nano-

particles in a Block Copolymer Template. *Macromolecules* **2006**, *39*, 4108−4114.
(26) Nose, S. A unified formulation of the constant temperature molecular dynamics methods. *J. Chem. Phys.* **1984**, *81*, 511−519.
(27) Hoover, W. G. Canonical dynamics: Equilibrium phase-space distributions. *Phys. Rev. A* **1985**, *31*, 1695−1697.
(28) Perdew, J. P.; Burke, K.; Ernzerhof, M. Generalized Gradient Approximation Made Simple. *Phys. Rev. Lett.* **1996**, *77*, 3865−3868.
(29) Troullier, N.; Martins, J. L. Efficient pseudopotentials for plane-wave calculations. *Phys. Rev. B* **1991**, *43*, 1993−2006.
(30) Humphrey, W.; Dalke, A.; Schulten, K. VMD: Visual Molecular Dynamics. *J. Mol. Graphics* **1996**, *14*, 33−38.
(31) Frisch, M. J.; Trucks, G. W.; Schiegel, H. B.; Scuseria, G. E.; Robb, M. A.; Cheeseman, J. R.; Montgomery, J. A., Jr.; Vreven, T.; Kudin, K. N.; Burant, J. C. *Gaussian 09*; Gaussian, Inc.: Pittsburgh, PA, 2009.
(32) Becke, A. D. Density-functional thermochemistry. III. The role of exact exchange. *J. Chem. Phys.* **1993**, *98*, 5648−5652.
(33) Lee, C.; Yang, W.; Parr, R. G. Development of the Colle-Salvetti correlation-energy formula into a functional of the electron density. *Phys. Rev. B* **1988**, *37*, 785−789.
(34) Polavarapu, P. L. Ab initio vibrational Raman and Raman optical activity spectra. *J. Phys. Chem.* **1990**, *94*, 8106−8112.
(35) Anderson, A. *The Raman Effect*; Marcel Dekker: New York, 1971; vol. *1*, chapter 2.
(36) Dutta, B.; Bhattacharjee, B.; Chowdhury, J. Physics behind the Barrier to Internal Rotation of an Acetyl Chloride Molecule: A Combined Approach from Density Functional Theory, Car−Parrinello Molecular Dynamics, and Time-Resolved Wavelet Transform Theory. *ACS Omega* **2018**, *3*, 6794−6803.
(37) Jung, H. S.; Kim, K.; Kim, M. S. Raman spectroscopic investigation of the adsorption of4-mercaptopyridine on a silver-sol surface. *J. Mol. Struct.* **1997**, *407*, 139−147.
(38) Hu, J.; Zhao, B.; Xu, W.; Li, B.; Fan, Y. Surface-enhanced Raman spectroscopy study on the structure changes of 4-mercaptopyridine adsorbed on silver substrates and silver colloids. *Spectrochem. Acta Part A* **2002**, *58*, 2827−2834.
(39) Saha, S.; Ghosh, M.; Chowdhury, J. Infused self-assembly on Langmuir−Blodgett Film: Fabrication of highly efficient SERS active substrates with controlled plasmonic aggregates. *J. Raman Spectrosc.* **2019**, *50*, 330−344.
(40) Chao, Y.; Zhou, Q.; Li, Y.; Yan, Y.; Wu, Y.; Zheng, J. Potential Dependent Surface-enhanced Raman Scattering of 4-Mercaptopyridine on Electrochemically Roughened Silver Electrodes. *J. Phys. Chem. C* **2007**, *111*, 16990−16995.
(41) Guo, H.; Ding, L.; Mo, Y. Adsorption of 4-mercaptopyridine onto laser-ablated gold, silver and copper oxide films: A comparative surface-enhanced Raman scattering investigation. *J. Mol. Struct.* **2011**, *991*, 103−107.
(42) Pagliai, M.; Muniz-Miranda, F.; Cardini, G.; Righini, R.; Schettino, V. Hydrogen Bond Dynamics of Methyl Acetate in Methanol. *J. Phys. Chem. Lett.* **2010**, *1*, 2951−2955.
(43) Muniz-Miranda, M.; Pagliai, M.; Muniz-Miranda, F.; Schettino, V. Raman and computational study of solvation and chemisorption of thiazole in silver hydrosol. *Chem. Commun.* **2011**, *47*, 3138−3140.
(44) Kirby, J. F.; Swain, C. J. Power spectral estimates using two dimensional Morlet-fan wavelets with emphasis on the long wavelengths: jackknife errors, bandwidth resolution and orthogonality properties. *Geo phys. J. Int.* **2013**, *194*, 78−99.
(45) Dutta Roy, S.; Ghosh, M.; Chowdhury, J. Near-Field Response on the Far-Field Wavelength-Scanned Surface-Enhanced Raman Spectroscopic Study of Methylene Blue Adsorbed on Gold Nano-colloidal Particles. *J. Phys. Chem. C* **2018**, *122*, 10981−10991.
(46) Le Ru, E. C.; Galloway, C.; Etchegoin, P. G. On the connection between optical absorption/extinction and SERS enhancements. *Phys. Chem. Chem. Phys.* **2006**, *8*, 3083−3087.
(47) Das, S. K.; Bhattacharya, T. S.; Chowdhury, J. Deciphering the near-field response with the far-field wavelength-scanned SERS spectra of 4-mercaptopyridine adsorbed on gold nanocolloidal particles entrapped in Langmuir Reverse Schaefer film of 5CB liquid crystal molecules. *Phys. Chem. Chem. Phys.* **2020**, *22*, 8719−8729.
(48) Das, S. K.; Saha, S.; Ghosh, M.; Chowdhury, J. How SERS responses of probe molecules depend on topographies of the substrates? A vis-à-vis exploration. *Vib. Spectrosc.* **2020**, *107*, 103031−103038.
(49) Chadha, R.; Das, A.; Debnath, A. K.; Kapoor, S.; Maiti, N. 2-thiazoline-2-thiol functionalized gold nanoparticles for detection of heavy metals, Hg(II) and Pb(II) and probing their competitive surface reactivity: A colorimetric, surface enhanced Raman scattering (SERS) and x-ray photoelectron spectroscopic (XPS) study. *Col. Surf. A* **2021**, *615*, 126279−126291.
(50) Caporali, S.; Muniz-Miranda, F.; Pedone, A.; Muniz-Miranda, M. SERS, XPS and DFT Study of Xanthine Adsorbed on Citrate-Stabilized Gold Nanoparticles. *Sensors* **2019**, *19*, 2700−2709.
(51) Gabka, G.; Bujak, P.; Giedyk, K.; Kotwica, K.; Ostrowski, A.; Malinowska, K.; Lisowski, W.; Sobczak, J. W.; Pron, A. Ligand exchange in quaternary alloyed nanocrystals − a spectroscopic study. *Phys. Chem. Chem. Phys.* **2014**, *16*, 23082−23088.
(52) Su, C.; Lu, Z.; Zhao, H.; Yang, H.; Chen, R. Photoinduced switchable wettability of bismuth coating with hierarchical dendritic structure between super hydrophobicity and super hydrophilicity. *Appl. Surf. Sci.* **2015**, *353*, 735−743.
(53) Desimoni, E.; Brunetti, B. X-Ray Photoelectron Spectroscopic Characterization of Chemically Modified Electrodes Used as Chemical Sensors and Biosensors: A Review. *Chemosensors* **2015**, *3*, 70−117.
(54) Park, J.-W.; Shumaker-Parry, J. S. Strong Resistance of Citrate Anions on Metal Nanoparticles to Desorption under Thiol Functionalization. *ACS Nano* **2015**, *9*, 1665−1682.
(55) Wang, Z.; Shen, X.; Yan, Y.; Qian, T.; Wang, J.; Sun, Q.; Jin, C. Facile fabrication of a PDMS @ stearic acid-Al$(OH)_3$ coating on lignocellulose composite with superhydrophobicity and flame retardancy. *Appl. Surf. Sci.* **2018**, *450*, 387−395.
(56) Li, C.; Xie, B.; He, Z.; Chen, J.; Long, Y. 3D structure fungi-derived carbon stabilized stearic acid as a composite phase change material for thermal energy storage. *Renewable Energy* **2019**, *140*, 862−873.
(57) Wang, Y.; Sun, Z.; Wang, Y.; Hu, H.; Zhao, B.; Xu, W.; Lombardi, J. R. Surface-enhanced Raman scattering on mercaptopyridine-capped CdS microclusters. *Spectrochem. Acta Part A* **2007**, *66*, 1199−1203.
(58) Zhang, H.-L.; Evans, S. D.; Henderson, J. R.; Miles, R. E.; Shen, T. Spectroscopic Characterization of Gold Nanoparticles Passivated by Mercaptopyridine and Mercaptopyrimidine Derivatives. *J. Phys. Chem. B* **2003**, *107*, 6087−6095.
(59) Herrera, S.; Tasca, F.; Williams, F. J.; Calvo, E. J.; Carro, P.; Salvarezza, R. C. Surface Structure of 4- Mercaptopyridine on Au (111): A New Dense Phase. *Langmuir* **2017**, *33*, 9565−9572.
(60) Liu, Q.; Liu, T.; Fang, Q. F.; Liang, F. J.; Wang, J. X. Preparation and characterization of nanocrystalline composites Mo−C−N hard films. *Thin Solid Films* **2006**, *503*, 79−84.
(61) Chen, D.; Wang, S.; Zhang, Z.; Quan, H.; Wang, Y.; Jiang, Y.; Hurlock, M. J.; Zhang, Q. Molten NaCl-induced MOF-derived carbon-polyhedron decorated carbon-nanosheet with high defects and high N-doping for boosting the removal of carbamazepine from water. *Environ. Sci.: Nano* **2020**, *7*, 1205−1213.
(62) Lamp, B. D.; Hobara, D.; Porter, M. D.; Niki, K.; Cotton, T. M. Correlation of the Structural Decomposition and Performance of Pyridinethiolate Surface Modifiers at Gold Electrodes for the Faciliation of Cytochrome c Heterogeneous Electron- Transfer Reactions. *Langmuir* **1997**, *13*, 736−741.
(63) Schoenfisch, M. H.; Pemberton, J. E. Air Stability of Alkenthiol Self- Assembled Monolayers on Silver and Gold Surfaces. *J. Am. Chem. Soc.* **1998**, *120*, 4502−4513.
(64) Kishore, K.; Dey, G. R.; Naik, D. B. Nature of transient species formed during pulse radiolysis of 4-mercaptopyridine in aqueous solutions: Formation of a dimer radical species by one-electron reduction reaction. *Res. Chem. Intermed.* **2002**, *28*, 29−39.

https://doi.org/10.1021/acsomega.1c07321
ACS Omega 2022, 7, 27818−27830

(65) Baldwin, J. A.; Vlckova, B.; Andrews, M. P.; Butler, I. S. Surface-Enhanced Raman Scattering of Mercaptopyridines and Pyrazinamide Incorporated in Silver Colloid−Adsorbate Films. *Langmuir* **1997**, *13*, 3744−3751.
(66) Fu, X.; Bei, F.; Wang, X.; Yang, X.; Lu, L. Surface-enhanced Raman scattering of 4-mercaptopyridine on sub-monolayers of α-Fe_2O_3 nanocrystals (sphere, spindle, cube). *J. Raman Spectrosc.* **2009**, *40*, 1290−1295.
(67) Baldwin, J.; Schuhler, N.; Butler, I. S.; Andrews, M. P. Integrated Optics Evanescent Wave Surface Enhanced Raman Scattering (IO-EWSERS) of Mercaptopyridines on a Planar Optical Chemical Bench: Binding of Hydrogen and Copper Ion. *Langmuir* **1996**, *12*, 6389−6398.
(68) Pradhan, M.; Chowdhury, J.; Sarkar, S.; Sinha, A. K.; Pal, T. Hierarchical Gold Flower with Sharp Tips from Controlled Galvanic 2 Replacement Reaction for High Surface Enhanced Raman Scattering 3 Activity. *J. Phys. Chem. C* **2012**, *116*, 24301−24313.
(69) Otto, A.; Billmann, J.; Eickmans, J.; Erturk, U.; Pettenkofer, C. The "adatom model" of SERS (Surface Enhanced Raman Scattering): The present status. *Surf. Sci.* **1984**, *138*, 319−338.
(70) Chadha, R.; Das, A.; Kapoor, S.; Maiti, N. Surface-induced dimerization of 2-thiazoline-2-thiol on silver and gold nanoparticles: A surface enhanced Raman scattering (SERS) and density functional theoretical (DFT) study. *J. Mol. Liq.* **2021**, *322*, 114536−114543.
(71) Ramirez, E. A.; Cortes, E.; Rubert, A. A.; Carro, P.; Benitez, G.; Vela, M. E.; Salvarezza, R. C. Complex Surface Chemistry of 4-Mercaptopyridine Self-Assembled Monolayers on Au (111). *Langmuir* **2012**, *28*, 6839−6847.
(72) Roy, D.; Furtak, T. E. Vibrational characteristics of silver clusters in surface-enhanced Raman scattering. *Phys. Rev. B Condens Matter.* **1986**, *34*, 5111−5117.
(73) Pagliai, M.; Caporali, S.; Muniz-Miranda, M.; Pratesi, G.; Schettino, V. SERS, XPS, and DFT Study of Adenine Adsorption on Silver and Gold Surfaces. *J. Phys. Chem. Lett.* **2012**, *3*, 242−245.
(74) Maiti, N.; Chadha, R.; Das, A.; Kapoor, S. Surface selective binding of 2,5-dimercapto-1,3,4-thiadiazole (DMTD) on silver and gold nanoparticles: a Raman and DFT study. *RSC Adv.* **2016**, *6*, 62529−62539.
(75) Muniz- Miranda, M.; Muniz-Miranda, F.; Pedone, A. Raman and DFT study of methimazole chemisorbed on gold colloidal nanoparticles. *Phys. Chem. Chem. Phys.* **2016**, *18*, 5974−5980.
(76) Choudhury, N. Dynamics of Water in Solvation Shells and Intersolute Regions of C60: A Molecular Dynamics Simulation Study. *J. Phys. Chem. C* **2007**, *111*, 2565−2572.
(77) Cauet, E.; Bogatko, S.; Weare, J. H.; Fulton, J. L.; Schenter, G. K.; Bylaska, E. J. Structure and dynamics of the hydration shells of the Zn^{2+} ion from ab initio molecular dynamics and combined ab initio and classical molecular dynamics simulations. *J. Chem. Phys.* **2010**, *132*, 194502−194514.
(78) Wang, X.; Toroz, D.; Kim, S.; Clegg, S. L.; Park, G.-S.; Di Tommaso, D. Density functional theory based molecular dynamics study of solution composition effects on the solvation shell of metal ions. *Phys. Chem. Chem. Phys.* **2020**, *22*, 16301−16313.
(79) Raucci, U.; Chiariello, M. G.; Rega, N. Modeling Excited-State Proton Transfer to Solvent: A Dynamics Study of a Super Photoacid with a Hybrid Implicit/Explicit Solvent Model. *J. Chem. Theory Comput.* **2020**, *16*, 7033−7043.
(80) Chowdhury, J.; Sarkar, J.; Tanaka, T.; Talapatra, G. B. Concentration-Dependent Orientational Changes of 2-Amino-2-thiazoline Molecule Adsorbed on Silver Nanocolloidal Surface Investigated by SERS and DFT. *J. Phys. Chem. C* **2008**, *112*, 227−239.
(81) Muniz-Miranda, M.; Muniz-Miranda, F.; Giorgetti, E. Spectroscopic and Microscopic Analyses of Fe_3O_4/Au Nanoparticles Obtained by Laser Ablation in Water. *Nanomaterials* **2020**, *10*, 132−144.

https://doi.org/10.1021/acsomega.1c07321
ACS Omega 2022, 7, 27818−27830